COUPLED RADIO AND X-RAY EMISSION AND EVIDENCE FOR DISCRETE EJECTA IN THE JETS OF SS 433

J. C. A. Miller-Jones[1,2]
NRAO Headquarters, 520 Edgemont Road, Charlottesville, Virginia, 22903

S. Migliari
Center for Astrophysics and Space Sciences, University of California San Diego, 9500 Gilman Dr., La Jolla, CA 92093

R. P. Fender[2]
School of Physics and Astronomy, University of Southampton, Highfield, Southampton, SO17 1BJ, UK

T. W. J. Thompson
Center for Astrophysics and Space Sciences, University of California San Diego, 9500 Gilman Dr., La Jolla, CA 92093

M. van der Klis
Astronomical Institute 'Anton Pannekoek', University of Amsterdam, Kruislaan 403, 1098 SJ, Amsterdam, The Netherlands

and

M. Méndez[2]
Kapteyn Astronomical Institute, Groningen University, 9700 AV, Groningen, The Netherlands
Draft version April 8, 2008

ABSTRACT

We present five epochs of simultaneous radio (VLA) and X-ray (*Chandra*) observations of SS 433, to study the relation between the radio and X-ray emission in the arcsecond-scale jets of the source. We detected X-ray emission from the extended jets in only one of the five epochs of observation, indicating that the X-ray reheating mechanism is transient. The reheating does not correlate with the total flux in the core or in the extended radio jets. However, the radio emission in the X-ray reheating regions is enhanced when X-ray emission is present. Deep images of the jets in linear polarization show that outside of the core, the magnetic field in the jets is aligned parallel to the local velocity vector, strengthening the case for the jets to be composed of discrete bullets rather than being continuous flux tubes. We also observed anomalous regions of polarized emission well away from the kinematic trace, confirming the large-scale anisotropy of the magnetic field in the ambient medium surrounding the jets.

Subject headings: Xrays: binaries – radio continuum: stars – stars: individual (SS 433) – ISM: jets and outflows – polarization

1. INTRODUCTION

SS 433 is one of the most persistent, stable, and well-studied sources of relativistic jets in the Galaxy. The system is a high-mass X-ray binary at a distance of 5.5 ± 0.2 kpc (Lockman, Blundell & Goss, 2007), accreting at a very high rate. The consequent high kinetic energy output in the jets has deformed the surrounding W 50 nebula (Begelman et al. 1980).

Precession of the jets in SS 433 is observed in both the Doppler-shifted X-ray (Watson et al. 1986) and optical (Margon et al. 1979) emission lines, at distances of $\sim 10^{11}$ and $\sim 10^{15}$ cm respectively from the centre of the system. Radio observations further confirm the precession scenario, with the radio jets tracing out a corkscrew pattern formed by the projection onto the plane of the sky of a sequence of ballistically-

moving knots ejected from a jet precessing about a fixed axis (Hjellming & Johnston 1981). The jet precession is well fit by the kinematic model (Abell & Margon 1979; Milgrom 1979; Fabian & Rees 1979), in which antiparallel jets precess about an axis inclined at $78.83°$ to the line of sight with a period of 162.5 d, a precession cone opening angle of $19.85°$, and a jet speed of $0.2602c$ (Stirling et al. 2002). The velocity of the jets has remained very stable since the original identification of the Doppler-shifted emission lines in the source spectrum (Margon et al. 1979), although there is evidence for small deviations from the mean velocity, of rms $0.014c$ (Blundell & Bowler 2005).

The polarization properties of the radio jets were studied in detail by Stirling et al. (2004). They found evidence for a depolarization region surrounding the core, outside of which the jets showed linear polarization of up to 20 per cent, with a magnetic field aligned parallel to the kinematic locus of the jets. Roberts et al. (2007) also examined the polarization properties of the jets, confirm-

Electronic address: jmiller@nrao.edu
[1] Jansky Fellow, National Radio Astronomy Observatory
[2] Astronomical Institute 'Anton Pannekoek', University of Amsterdam, Kruislaan 403, 1098 SJ, Amsterdam, The Netherlands

ing the depolarization region and the alignment of the magnetic field with the local jet direction within 1 arcsec of the core. They also noted the presence of anomalous highly-polarized emission off the kinematic trace, indicating that the magnetic fields in the ambient medium should be highly ordered on scales of thousands of AU, possibly due to interactions with the jet and subsequent shearing of the existing field. Stirling et al. (2004) interpreted the alignment of the magnetic field with the local jet direction as evidence that the jet was a continuous plasma tube, rather than being composed of discrete radio-emitting plasmons.

Arcsecond-scale X-ray jets were first observed in SS 433 by Marshall, Canizares & Schulz (2002), and Migliari, Fender & Méndez (2002) detected highly-ionised, Doppler-shifted iron lines at distances of 10^{17} cm from the binary core, implying reheating of baryonic matter to temperatures in excess of 10^7 K downstream in the jets. The X-ray jets do not have a static, long-term structure, but vary on timescales as short as days, if not hours. There is no correlation between the X-ray emission and the precession phase of the jets (Migliari et al. 2005). The emission was initially explained as internal shocks arising from velocity variations in the ejecta energising the flow downstream in the jets (Migliari et al. 2002). Stirling et al. (2004) proposed an alternative explanation for the X-ray reheating, invoking the model of Heavens, Ballard & Kirk (1990), whereby sideways ram pressure on the plasma tube could give rise to shocks which energised the plasma. However, Migliari et al. (2005) observed rapid variability, whereby two knots on different parts of the precession trace brightened sequentially, which they ascribed to energisation by a faster underlying flow of $\sim 0.5c$. Such unseen, highly-relativistic flows have recently been inferred to exist in the Galactic neutron star X-ray binaries Scorpius X-1 (Fomalont et al. 2001) and Circinus X-1 (Fender et al. 2004). An underlying flow propagating outwards at high speed energises the mildly-relativistic radio-emitting regions further downstream in the flow, lighting them up via shock heating.

2. OBSERVATIONS AND DATA REDUCTION

In order to test the hypothesis of a fast, unseen flow energising the flow downstream in the jets, we proposed for a sequence of four simultaneous 10-ks observations with *Chandra* and the Very Large Array (VLA), to track the evolution of the thermal and non-thermal components of the emitting regions. The High Resolution Camera (HRC) on board *Chandra* was used, to maximise the spatial (< 0.5 arcsec) and temporal ($16\,\mu$s) resolution, thus avoiding pile-up and enabling us to identify and track the motions of individual jet knots. The observing frequency in the radio band was chosen in order to best match the spatial resolution of *Chandra*.

The observations were spaced over the course of 8 days in 2006 February, and the radio and X-ray properties are summarised in Tables 1 and 3. We also re-analysed archival radio and X-ray data from July 2003, in order to investigate for the first time the balance of thermal and non-thermal emission from the arcsecond-scale X-ray jets.

2.1. *Radio*

In both the observations of 2003 July and those of 2006 February, we observed SS 433 at 4.86 GHz with the VLA in its A-configuration. Table 1 shows the observation dates and durations for each epoch. The observing bandwidth was 50 MHz. The primary calibrator was 3C 286, and the secondary calibrator was J 1922+1530. The flux density scale used was that derived at the VLA in 1999 as implemented in the 2004 December 31 version of AIPS. In the observations of 2003 July, the parallactic angle coverage of J 1922+1530 was sufficient to calibrate the polarization leakage terms, whereas in February 2006 the calibrator 3C 84 was used for this part of the calibration (except on 2006 February 19, when it was not observed and no polarization calibration was possible). In all cases, 3C 286 was used to calibrate the absolute polarization position angle. External gain and polarization calibration were automated using PARSELTONGUE, a Python interface to AIPS. Self-calibration and imaging were then carried out manually, following standard procedures within AIPS.

2.2. *X-ray*
2.2.1. *ACIS*

The 60-ks ACIS-S observation of 2003 July 10–11 (MJD 52830–52831), previously analysed by Migliari et al. (2005), shows two X-ray extensions, east and west from the heavily piled-up core (Fig. 1). We estimated the 0.5–10 keV spectrum of the core by analyzing the photons in the readout streak, which should be unaffected by pile-up. We extracted the background-subtracted spectrum in a rectangular region with 280×20 pixels covering the readout streak, and corrected it with the effective exposure time for the readout streak data (see Migliari et al. 2005 for details). We show the spectrum of the core in Fig. 2. The spectrum is well fitted with a model consisting of an absorbed power law, with photon index $\sim$ 1.6, two Gaussian emission lines at $\sim$ 6.2 and $\sim$ 6.7 keV, and an absorption edge around 1.3 keV (at a significance of 7.4σ), obtaining a reduced $\chi^2 = 1.21$ with 172 d.o.f. (Table 2). The core flux, i.e. the flux in the readout streak spectrum corrected for the effective exposure time, is 7.1×10^{-10} erg cm^{-2} s^{-1}.

To extract the spectra of the X-ray jets, we selected two regions of size 1.46×1.98 arcsec^2, east and west of the core, as shown in Fig. 1. We extracted the 0.5–10 keV energy spectra in these two regions and subtracted the contribution of the core due to the tail of the point spread function (PSF). To do so, we created the PSF of a point source, using the PSF shape for photons at roughly the average energy of the spectrum, i.e. 3 keV, and with a count rate normalized to that estimated from the analysis of the readout streak. We chose the core-tail regions to subtract, such that in the PSF image their counts were equal to those in the jet region. In Fig. 3, we show the core-tail subtracted spectrum of the eastern jet, re-binned with a minimum of 40 counts per energy channel. The eastern jet spectrum is well fitted, with a reduced χ^2 of 1.12 (58 d.o.f.), using an absorbed bremsstrahlung model with a temperature of $\sim$ 10 keV and a marginally-detected Gaussian emission line around 6.7 keV (the normalization with 1σ error bars was $4.7^{+2.1}_{-1.6} \times 10^{-6}$ photons cm^{-2} s^{-1}). Given the broadening

TABLE 1
RADIO PROPERTIES OF THE JETS OF SS 433. PRECESSIONAL PHASE IS DEFINED ACCORDING TO THE CONVENTION OF STIRLING ET AL. (2002), WHEREBY $\phi = 0, 1, 2, ...$ CORRESPONDS TO THE EASTERN JET HAVING MAXIMUM REDSHIFT. COLUMN 3 GIVES THE FLUX DENSITY OF THE CORE AT EACH EPOCH, COLUMN 4 THE TOTAL INTEGRATED FLUX DENSITY OF THE CORE AND EXTENDED JETS TAKEN TOGETHER, AND COLUMNS 5 AND 6 THE TOTAL INTEGRATED FLUX DENSITY, I, WITHIN THE EASTERN AND WESTERN REGIONS SHOWN IN FIG. 1. COLUMNS 7 AND 8 GIVE THE TOTAL INTEGRATED POLARIZED FLUX DENSITY, P, FOR THOSE SAME EASTERN AND WESTERN REGIONS, AND COLUMNS 9 AND 10 GIVE THE AVERAGE FRACTIONAL POLARIZATIONS, $< F >= P/I$, WITHIN THOSE REGIONS. THE QUOTED UNCERTAINTIES ON THE FLUX DENSITIES ARE JUST THE STATISTICAL UNCERTAINTIES DUE TO THE RMS NOISE IN THE IMAGES. THERE IS A FURTHER SYSTEMATIC UNCERTAINTY IN THE ABSOLUTE FLUX CALIBRATION, BELIEVED TO BE OF ORDER 1–2 PER CENT.

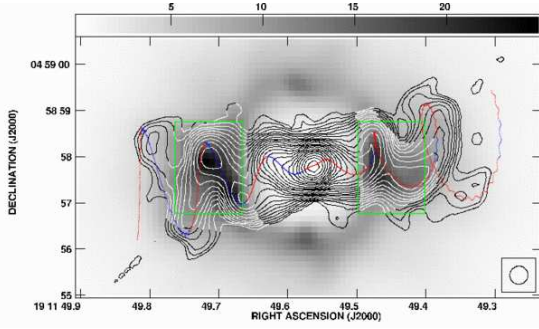| Date (MJD)	Phase	Core (mJy bm^{-1})	Flux densities Jet (integrated) mJy	East mJy	West mJy	Polarized flux densities East mJy	West mJy	Fractional polarization East	West
52831.29 ± 0.22	0.94	307.2 ± 0.02	474.5 ± 0.7	14.2 ± 0.3	23.1 ± 0.3	3.0 ± 0.1	2.8 ± 0.1	0.21 ± 0.01	0.12 ± 0.01
53785.80 ± 0.08	0.82	525.6 ± 0.06	667.1 ± 0.5	7.8 ± 0.6	9.9 ± 0.6	-	-	-	-
53787.76 ± 0.08	0.83	472.1 ± 0.03	623.7 ± 1.0	6.9 ± 0.4	8.7 ± 0.4	1.3 ± 0.3	1.2 ± 0.3	0.19 ± 0.04	0.14 ± 0.03
53790.83 ± 0.07	0.85	484.8 ± 0.03	636.6 ± 1.3	6.4 ± 0.4	9.2 ± 0.4	0.9 ± 0.2	0.9 ± 0.2	0.14 ± 0.04	0.10 ± 0.03
53793.68 ± 0.07	0.87	539.0 ± 0.03	716.3 ± 1.1	7.1 ± 0.4	9.3 ± 0.4	1.2 ± 0.3	1.0 ± 0.3	0.17 ± 0.05	0.11 ± 0.04

FIG. 1.— *Chandra* ACIS-S X-ray greyscale image of the 60-ks observation of 2003 July with radio contours superposed. The intensity wedge shows the ACIS-S count rates in counts s^{-1}. Total intensity contours are at levels of $\pm(\sqrt{2})^n$ times $19.8\,\mu$Jy bm^{-1}, where $n = 4, 5, 6, ...$. The maximum flux density in the image is 307 mJy beam^{-1}. The restoring beam, shown in the lower right of the image, is 0.40×0.39 arcsec^2 in PA $-25°5$. The calculated kinematic model precession trace, including nodding, has been overlaid. Red and blueshifted ejecta are indicated by their respective colours. The two green boxes show the X-ray extraction regions.
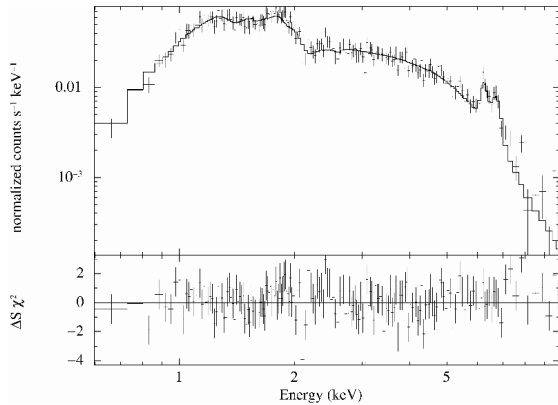

FIG. 2.— Spectrum of the core during the *Chandra* ACIS-S observation of 2003 July 10–11, extracted from the readout streak. The normalization shown is not corrected for the effective exposure time. The spectrum of the core is well fitted with a power-law model, an absorption edge at 1.3 keV, and two iron emission lines at ~ 6.2 and ~ 6.7 keV (see Section 2.2.1).
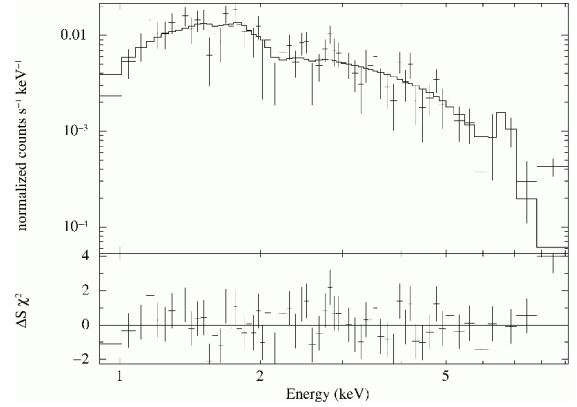

FIG. 3.— Core-PSF subtracted spectrum of the eastern jet region during the *Chandra* ACIS-S observation of 2003 July 10–11. The continuum is well fitted with either a 10-keV bremsstrahlung continuum (shown here) or a power-law component. The iron emission line at ~ 6.7 keV is marginally significant (see Section 2.2.1).

of the PSF at higher energies, we note that the use of a 6.7-keV PSF reduces the line strength by about a factor of two. We obtained an equally good fit with an absorbed power-law model ($\Gamma = 1.7 \pm 0.3$), and cannot distinguish between the bremsstrahlung and power-law models with the current data. We note that the emission line around 6.2 keV present in the spectrum of the core (Fig. 2) disappears completely. Freezing the 6.7-keV line parameters and adding an extra line to the model, with the energy and width set to 6.2 and 0.07 keV respectively (as found in the core), gave an upper limit to the normalization of 6.7×10^{-7} photons cm^{-2} s^{-1}. The corresponding upper limit to the flux in the line is $< 6.7 \times 10^{-15}$ erg cm^{-2} s^{-1}. The 2–10 keV flux in the eastern jet region is 3.5×10^{-13} erg cm^{-2} s^{-1}. The best-fitting parameters of this model are shown in Table 2. The flux estimate for the western X-ray jet region, being very close to the core, is more difficult to constrain due to the high pile-up. Its core-tail subtracted energy spectrum is well fitted with a simple absorbed bremsstrahlung model with a temperature of ~ 3 keV and has a 2-10 keV flux upper limit (98 per cent confidence) of 2.6×10^{-13} erg cm^{-2} s^{-1} (see Table 2).

2.2.2. *HRC*

TABLE 2
BEST-FIT PARAMETERS OF THE 0.5–10 keV ENERGY
SPECTRA IN THE READOUT STREAK, EAST AND WEST
REGIONS OF THE 2003 JULY *Chandra*/ACIS-S
OBERVATION.

	Core	East	West
$N_{\rm H}$	0.79 ± 0.02	0.9 ± 0.1	1.9 ± 0.6
Γ	1.48 ± 0.02	1.7 ± 0.3	–
$N_{\rm pl}$	4.0 ± 0.2	$0.87^{+0.45}_{-0.25}$	–
$kT_{\rm br}$	26 ± 4	$10.0^{+5.2}_{-2.5}$	3.1 ± 1.8
$N_{\rm br}$	57 ± 1	9.7 ± 0.9	<15
$E_{\rm g1}$	$6.23^{+0.07}_{-0.03}$	6.2	–
σ_1	0.08 ± 0.02	0.07	–
N_{g1}	12 ± 2	<0.67	–
$E_{\rm g2}$	6.68 ± 0.03	6.7 ± 0.1	–
σ_2	$0.17^{+0.41}_{-0.04}$	<0.3	–
$N_{\rm g2}$	19 ± 3	$4.7^{+3.4}_{-2.7}$	–
$E_{\rm edge}$	1.35 ± 0.02	–	–
τ	0.37 ± 0.05	–	–
F_X	7.1×10^{-10}	3.5×10^{-13}	$<2.6\times10^{-13}$
χ^2/d.o.f.	$208/172$	$65/58$	$61/40$

NOTE. — The parameters are: equivalent hydrogen column density $N_{\rm H}$ (in units of $10^{22}\,{\rm cm}^{-2}$), power law normalization $N_{\rm pl}$ (in units of 10^{-4} photons keV^{-1} cm^{-2} s^{-1} at 1 keV) and photon index Γ, bremsstrahlung temperature $kT_{\rm br}$ (in keV) and normalization $N_{\rm br}$ (in units of $(3.02 \times 10^{-20}/(4\pi D^2)) \int n_e n_i dV$, where D is the source distance (cm), and $n_{\rm e}$ and $n_{\rm i}$ are the electron and ion densities (cm^{-3})), Gaussian emission line peak energy $E_{\rm g}$ (in keV), Gaussian line width $\sigma_{\rm g}$ (in keV) and normalization N$_{\rm g}$ (in 10^{-6} photons cm^{-2} s^{-1} in the line), absorption edge energy threshold $E_{\rm edge}$ (in keV) and maximum absorption factor at threshold τ (in keV), and total X-ray flux F_X (in erg cm^{-2} s^{-1}). In the readout streak the normalizations of the model components have not been corrected for the effective exposure time. Note that, due to the proximity of the heavily piled-up core, the spectrum of the west region is not well constrained.

For the four HRC observations of 2006 February (Fig. 4), we extracted the counts in the same east and west regions used in the 2003 July ACIS observation. To estimate the contribution of the core, we created the normalized PSF of each image and extracted the counts in those same east and west regions. The PSF subtracted count rates of the east and west regions for the four HRC observations are shown in Table 3. There was no clear evidence in the HRC observations for jet-like extended emission as seen in the ACIS image, although the count rate was not consistent with zero. The images (Fig. 4) showed slightly enhanced diffuse emission in the E-W direction, possibly due to scattering of the core emission from the denser material along the jet direction. Other than this, the source was consistent with being an unresolved, variable point source. Since the peak sensitivity of the HRC is in the energy range 0.2–2 keV, the ACIS images of 2003 July were remade, using only the 0.5–

2 keV energy range. The arcsecond-scale X-ray jets were still present in this low-energy data from 2003 July, ruling out the possibility that the extension was only present in hard X-rays (> 2 keV).

To facilitate comparison of the measured X-ray count rates with earlier observations, we converted the measured HRC 0.1–10 keV count rates to those that would have been measured by HETGS (0.8–8 keV) and ACIS-S (0.5-10 keV). For this we used PIMMS with a model consisting of a power law with photon index $\Gamma = 1.66$ (the mean of the parameters derived for the HETGS observations by Migliari et al. (2005)), affected by interstellar absorption with $N_{\rm H} = 1 \times 10^{22}\,{\rm cm}^{-2}$.

2.2.3. *The nature of the iron line*

At the time of the 2003 July observation, the precessional phase was 0.94 (in the convention that phase 0, 1, 2,... correspond to the point at which the eastern jet is maximally redshifted). This would predict redshifts of 0.001 and 0.073 in the western and eastern jets respectively. This would make the two lines seen in the core spectrum (Table 2) consistent with the red and blueshifted Fe XXV 1s2p-1s^2 transition (rest energy 6.68 keV); the redshifts derived from the precessional phase would predict 6.68 and 6.23 keV respectively. Since the western jet has redshift 0.001, this line would be blended with emission from the same line in the stationary core, explaining both the higher normalization and broader line profile of the 6.68 keV line. We note that this transition (rest wavelength 1.855 Å) was also the most prominent line seen in the HETGS observations of Marshall et al. (2002), albeit at a different orbital phase and hence with different redshifts in the jets, lending further credence to our interpretation of the line as highly-ionised iron.

The iron line in the extended emission in the eastern jet is less easy to identify. The X-rays are spatially extended, so from the position of the extraction box (Fig. 1), the redshift could lie anywhere between -0.11 and 0.08 (the maximum possible blueshift and redshift for the eastern jet), giving a rest energy between 5.96 and 7.24 keV. However, Fig. 1 shows that the X-ray emission is strongest along the blueshifted part of the trace, and the location of the X-ray bright spots are both close to the transition between blueshift and redshift. If the line emission traces the continuum, we can rule out any redshift, so the rest frequency of the line would be ≤ 6.7 keV. The kinematic model calculations for the positions of the X-ray hotspots suggest that any blueshift is ≥ -0.04. We can thus rule out the 7.06 keV Fe XXV kβ line seen by Migliari et al. (2002), although both the neutral Fe-K line (6.40 keV), and the Fe XXV line seen in the core spectrum are plausible candidates. With such a marginal line detection however, we caution against over-interpreting this result.

3. THE RADIO IMAGES

3.1. *The kinematic model trace*

To calculate the kinematic model predictions, we used the published parameters of Stirling et al. (2002), but with the velocity and distance derived by Blundell & Bowler (2004), $0.2647c$ and 5.5 kpc respectively. We note that the phase reference time quoted
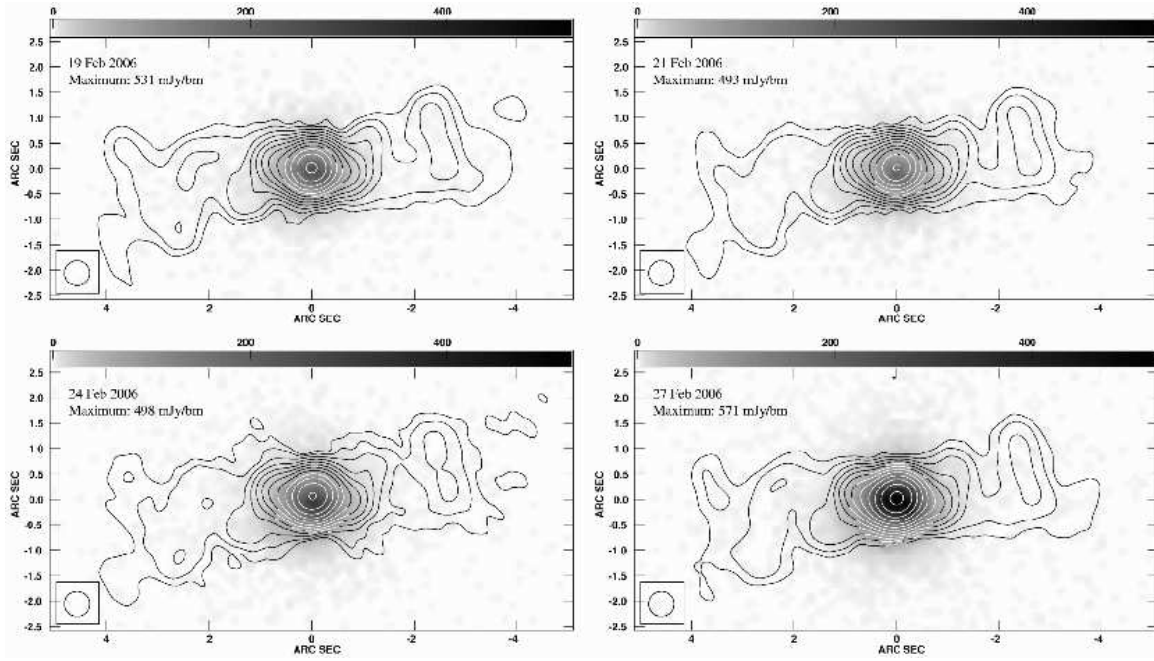
Fig. 4.— *Chandra* HRC greyscale images from 2006 February, with radio contours overlaid. The intensity wedges (all set to the same minimum and maximum) show the total counts from each HRC observation. Total intensity contours are at levels of $\pm 2^n$ times a representative rms noise level of $46\,\mu\text{Jy bm}^{-1}$, where $n = 5, 6, 7, \ldots$. The maximum total intensity in each image is given in the top left-hand corner. All images have been restored with the same beamsize of 0.49×0.49 arcsec^2 (shown in the lower right corner of each image). There is no evidence for any X-ray extension along the jet direction in any case. The X-ray core gets brighter over the course of the last three observations.

TABLE 3

NET COUNT RATES (AFTER PSF SUBTRACTION) OF THE HRC OBSERVATIONS IN THE EXTRACTION REGIONS OF THE CORE, EASTERN AND WESTERN JETS OF SS 433. THE 0.1–10 keV HRC COUNT RATES HAVE BEEN CONVERTED TO THE 0.8–8 keV HETGS AND 0.5–10 keV ACIS-S COUNT RATES, FOR COMPARISON WITH THE COUNT RATES DERIVED BY MIGLIARI ET AL. (2005).

Date (MJD)	Instrument	Core HRC s^{-1})	Core HETGS (s^{-1})	Core ACIS (s^{-1})	Eastern Jet HRC (10^{-3} s^{-1})	Eastern Jet HETGS (10^{-3} s^{-1})	Eastern Jet ACIS (10^{-3} s^{-1})	Western jet HRC (10^{-3} s^{-1})	Western jet HETGS (10^{-3} s^{-1})	Western jet ACIS (10^{-3} s^{-1})
51444	HETGS		1.442			3.6 ± 1.4				
51876	HETGS		0.557			18.3 ± 1.3				
51984	HETGS		1.876			24.6 ± 2.1				
52037	HETGS		0.363			23.4 ± 1.3				
52039	HETGS		0.234			25.4 ± 1.4				
52041	HETGS		0.846			23.8 ± 1.7				
51722	ACIS-S			2.3			43.7 ± 2.5			
52830	ACIS-S			8.8			27.8 ± 1.1			< 1.2
53785	HRC	0.753 ± 0.007	0.610	3.1	3.72 ± 0.84	3.016	15.44	8.07 ± 1.27	6.542	33.49
53787	HRC	0.568 ± 0.006	0.460	2.4	4.47 ± 0.76	3.624	18.55	8.54 ± 1.08	6.923	35.44
53790	HRC	0.997 ± 0.008	0.808	4.1	4.38 ± 0.90	3.551	18.18	7.31 ± 1.29	5.926	30.34
53793	HRC	1.816 ± 0.011	1.472	7.5	4.80 ± 1.22	3.891	19.92	11.60 ± 1.57	9.403	48.14

by Stirling et al. (2002) is in TJD rather than MJD, so it should read MJD 48615.5, for the point at which the eastern jet is maximally redshifted. With these parameters, the predicted trace appeared to overlay the data well, as seen in Figs. 1, 5, 6, and 7. We saw no need to invoke a quarter-period phase delay, a deceleration or a slow jet, as suggested by Stirling et al. (2004).

The left column of Fig. 5 shows the total intensity contours and radio polarization measurements (where polarization calibration was available) for all four epochs of observation during 2006 February, with the fitted kinematic model trace for each epoch overlaid. There is no significant evidence for the successive brightening of knots along the kinematic trace suggested by Migliari et al. (2005). This suggests that any underlying relativistic flow within the jets is not persistent. The rise in the core flux density over the course of the last three epochs of observation (Table 1), taken together with the rising X-ray count rate of the core, suggests that a new phase of activity and jet heating might have been beginning at this time.

3.2. *Polarization*

Stirling et al. (2004) studied the polarization properties of the arcsecond-scale radio jets of SS 433 and found a depolarization region surrounding the core of extent ~ 0.5 arcsec at 5 GHz. They derived a mean value
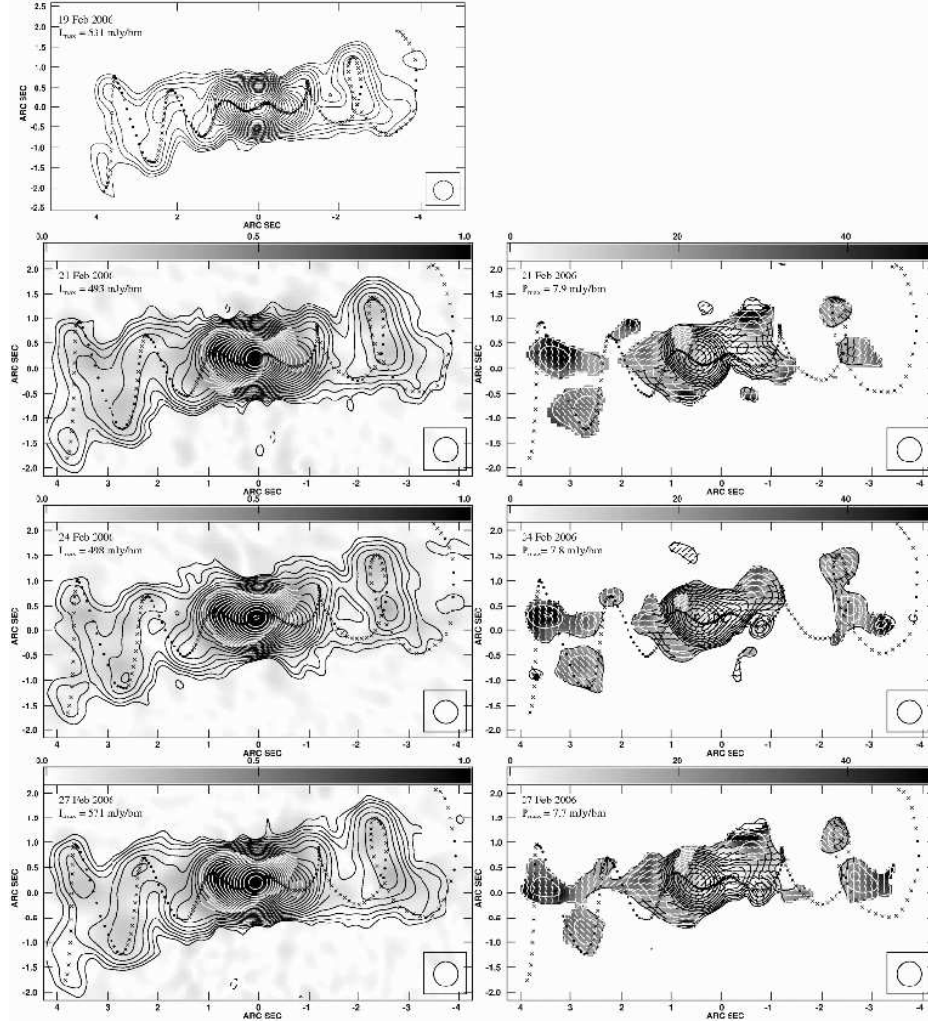
FIG. 5.— Radio images of SS 433 in 2006 February. Left column shows total intensity contours superposed on polarized intensity greyscale. Total intensity contours are at levels of $\pm(\sqrt{2})^n$, with $n = 5, 6, 7, ...$ times the noise level in the individual images (47.1, 35.4, 47.3 and 32.7 μJy bm^{-1} respectively), and the greyscale intensity wedge gives the polarized intensity in mJy. Right column shows polarized intensity contours superposed on fractional polarization greyscale ($F = P/I$), with polarization vectors showing the EVPA. Polarization vectors are of uniform length and have been rotated by $-25.9°$ to correct for Faraday rotation. The strength of polarization is given by the contours, which are at levels of $\pm(\sqrt{2})^n$ times the noise level in the polarized images (27, 24 and 26 μJy bm^{-1} respectively), where $n = 5, 6, 7, ...$ The greyscale intensity wedge is in per cent. The date and maximum intensity of each image are given in the top left-hand corner. All images have been restored with the same beamsize of 0.49×0.49 arcsec^2 (shown in the lower right corner of each image). The calculated precession trace for each date, including the nodding parameters given by Stirling et al. (2002), has been overlaid. Red and blueshifted ejecta are indicated by crosses and filled circles respectively.

of the rotation measure (RM) towards the source of 119 ± 16 rad m^{-2}, which increased to ~ 300 rad m^{-2} close to the radio core.

The right column of Fig. 5 shows the derived fractional polarization and electric vector position angles (EVPAs) for each of the epochs of observation in 2006 February where polarization data were available. The polarization vectors have been rotated clockwise by $25.9°$, to compensate for the rotation measure of 119 ± 6 rad m^{-2} found by Stirling et al. (2004). The images have all been convolved with the same circular restoring beam, to facilitate comparisons. The fractional polarization (greyscale), is shown only for the regions where both the total intensity and the linear polarization were more significant than 5σ. Fractional polarizations of up to 30 per cent are seen along the jets.

The linear polarization image of 2003 July 11, shown

in Fig. 7, confirms the depolarization of the core. Moving outwards, the fractional polarization then levels off at 20–30 per cent along the rest of the jet until the signal drops below the noise level. The high degree of polarization confirms the radio emission to be of synchrotron origin, ruling out thermal free-free emission as a viable emission mechanism.

3.2.1. Magnetic field orientation

With our deep image of 2003 July 11 (Figs. 6 and 7), whose rms of $19.8\,\mu$Jy bm^{-1} is a factor 3.5 lower than the 5-GHz observation of Stirling et al. (2004), we can more accurately measure the magnetic field direction along the jet. Fig. 8 shows the magnetic field directions inferred from the assumption that the field direction is perpendicular to the EVPA.

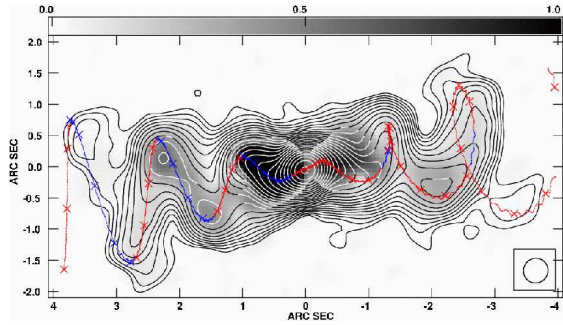From about half a period downstream of the core (cor-

FIG. 6.— Total intensity contours of 2003 July superposed on linear polarization greyscale. Total intensity contours are at levels of $\pm(\sqrt{2})^n$ times the noise level of $19.8\,\mu\,$Jy$\,$bm^{-1}, where $n = 5, 6, 7, ...$. The greyscale intensity wedge is in mJy$\,$beam^{-1}. The maximum flux density in the image is $307\,$mJy$\,$beam^{-1}. The restoring beam, shown in the lower right of the image, is $0.40 \times 0.39\,$arcsec^2 in PA $-25^{\circ}.5$. The calculated precession trace for each date, including the nodding parameters given by Stirling et al. (2002), has been overlaid. Red and blueshifted ejecta are indicated by their respective colours. The crosses along the trace mark ejecta separated by 20 d.
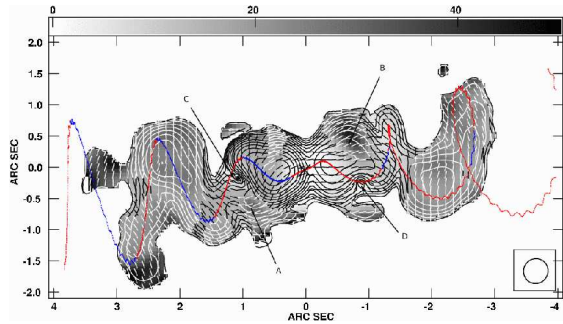

FIG. 7.— Linear polarization contours of 2003 July superposed on fractional polarization greyscale with EVPA vectors overlaid. The polarization vectors have been rotated by -25.9° to correct for the Faraday rotation due to the global RM of $119\,$rad$\,$m^{-2}. The magnetic field is perpendicular to the EVPAs. The polarization vectors are all of uniform length. The strength of polarization is given by the contours, which are at levels of $\pm(\sqrt{2})^n$ times the noise level in the polarized image of $10.3\,\mu\,$Jy$\,$bm^{-1}, where $n = 5, 6, 7, ...$. The greyscale intensity wedge is in per cent. The maximum polarized flux density in the image is $4.5\,$mJy$\,$beam^{-1}. The restoring beam, shown in the lower right of the image, is $0.40 \times 0.39\,$arcsec^2 in PA $-21^{\circ}.3$. The calculated precession trace for each date, including the nodding parameters given by Stirling et al. (2002), has been overlaid. Red and blueshifted ejecta are indicated by their respective colours. The central cross marks the position of the radio core (maximum total intensity).

responding to a distance of $\sim 0.7\,$arcsec) in the approaching jet and one full period in the receding western jet (where the rotation measure is greater), the implied magnetic field direction is extremely well-aligned parallel to the local velocity vector. This is in contrast to the work of Stirling et al. (2004), who suggested that the field was aligned along the kinematic model locus out to ~ 1.5 precession periods ($\sim 2.5\,$arcsec) from the core. Closer to the central binary system, this correlation clearly breaks down. However, since the EVPAs have only been corrected for the global foreground Faraday rotation of $119\,$rad$\,$m^{-2}, the true EVPA close to the core will be smaller than the measured values. This effect is noticeable further out in the receding (western) jet than in the approaching (eastern) jet, consistent with the results
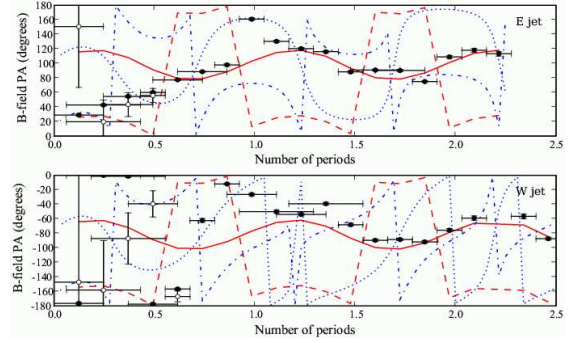

FIG. 8.— Plots of the variation of the magnetic field direction with position away from the core along the kinematic model trace. The magnetic field direction has in all cases been assumed to be perpendicular to the Faraday rotation-corrected EVPA. Filled circles are for Faraday derotation with the global RM of $119\,$rad$\,$m^{-2} and open circles use the RMs derived from a fit to the data of Roberts et al. (2007). Red solid and dashed lines show the predictions of the kinematic model for the directions parallel and perpendicular to the local velocity vector respectively. Blue dotted and dot-dashed lines show the directions along and perpendicular to the local jet direction (the projection of the kinematic model trace on the plane of the sky) respectively. All field directions have a 180° ambiguity, and the model traces have been wrapped by 180° where necessary. The top plot shows the approaching (eastern) jet and the bottom plot is for the western (receding jet). The measured points far enough away from the core correlate well in both jets with the solid line tracing the local velocity vector (the direction of motion of the ballistically-moving ejecta).

of Roberts et al. (2007), whose figure 11 demonstrates clearly that the fitted rotation measure in the western jet exceeds that in the eastern jet out to $\sim 0.9\,$arcsec from the core. However, using their fitted RMs does not bring the implied magnetic field direction back to alignment with the local jet velocity (see the white points in Fig. 8). The source is optically thin down to $\sim 30\,$mas from the central binary (Paragi et al. 1999), so the deviation from the correlation close to the core cannot be explained by the transition from the case where the magnetic field is aligned perpendicular to the EVPA to one where it is parallel, as occurs on moving from an optically thin to thick regime. We note that Roberts et al. (2007) found that the magnetic field between ~ 0.4 and $1\,$arcsec of the core appeared to follow the kinematic model trace, becoming perpendicular to the trace in the very inner regions (although with such a small fractional polarization in the central regions, this result was not deemed to be secure). Higher-resolution observations at multiple frequencies are required to determine whether the magnetic field orientation really changes along the jets.

The images of 2006 February are less deep, such that we cannot reliably measure the polarization and magnetic field orientation all along the kinematic trace. However, the observed EVPA orientations in the outer parts of the jets (Fig. 5) also appear to be perpendicular to the direction radially outwards from the core, suggesting that the alignment of the magnetic field with the local velocity vector is persistent.

3.2.2. *Anomalous polarized emission*

The polarized intensity does not follow the total intensity (and hence the kinematic trace) perfectly. Regions A and B in Fig. 7 show high linear and fractional polarization and are well off the kinematic model trace.

Regions C and D, on the contrary, lie directly on the kinematic model trace, and show very low linear and fractional polarization, which can not be explained by beam depolarization due to the kinematic model covering a full rotation in those regions. Region C corresponds to the discrepant point in the top plot of Fig. 8, at 0.98 periods, so the low fractional polarization seems to be related to the anomaly in magnetic field direction.

We note that regions A and B correspond well to knots 1 and 2 identified in figure 13 of Stirling et al. (2004). These knots, and also the anomalous knots observed by Spencer & Waggett (1984), appear at the point in the precession trace where the jet makes its first significant bend. Similar features are also seen in the polarization images of the 2006 February observations (Fig. 5). From Fig. 8, this ($\sim$ 0.4 periods downstream from the core; see Fig. 8) is just after the point at which there is a local maximum in the angle between the local velocity vector and the local jet direction (solid and dotted lines). The Faraday-derotated EVPAs in these regions are aligned pointing back towards the core, implying that the magnetic field is perpendicular to the velocity, if these regions have a velocity away from the central binary. This could be caused by compression of the magnetic field at a shock front moving outwards (e.g. Stirling et al. 2004; Heavens et al. 1990), although the origin of such a shock remains unclear. Roberts et al. (2007) also found highly-polarized off-jet emission on the inner side of the first bend in the jet, which they ascribed to large-scale shearing motions in the ambient medium close to the jets. Either way, such structures are clearly not unusual in this system.

4. COMPARISON OF RADIO AND X-RAY DATA

No extended X-ray emission was seen in the observations of 2006 February, and there was no evidence in the radio images for a series of knots along the precession trace brightening sequentially. We are thus unable to verify the scenario of a faster-moving shock lighting up individual knots as it passes (Migliari et al. 2005). If such a fast, unseen flow exists, it was not present during the course of these observations, and further monitoring is required when extended X-ray jets are present, to verify this scenario.

The only observation in which both radio and X-ray emission were observed from the arcsecond-scale jets was that of 2003 July. Before a comparison could be made, the two sets of images were reprojected to the same geometry using the AIPS task OHGEO. While the SIN projection is common in radio aperture synthesis, the *Chandra* data used the TAN projection, necessitating a reprojection of the radio image before creating the overlay shown in Fig. 1 (see Greisen (1983) for further details). This Figure shows that the X-ray emitting regions lie on the kinematic model trace, and correlate well with the radio emission from the jet.

4.1. *The broadband spectrum*

Since a fit to the X-ray spectrum cannot significantly distinguish between power-law and bremsstrahlung emission, we cannot determine the emission mechanism from the X-ray data alone. A synchrotron spectrum with a spectral index of -0.7 to -0.8 ($S_\nu \propto \nu^\alpha$) seems to be consistent with the overall radio to X-ray spectrum (Fig. 9),
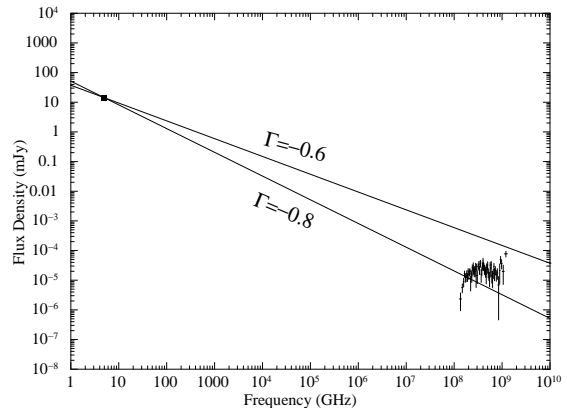

FIG. 9.— Broadband radio to X-ray spectrum of the eastern X-ray jet region for 2003 July. Power law spectra of spectral index -0.6 and -0.8 have been overlaid, demonstrating the need for accurate radio spectral indices to help constrain the nature of the X-ray emission.

and with the power-law fit to the X-ray data. Our single-frequency radio observations do not allow us to empirically determine the spectral index. Previous authors (Vermeulen et al. 1993; Stirling et al. 2004) have measured spectral indices of between -0.6 and -0.8 in the extended jets outside the core region, which would be consistent with a single spectrum running from the radio to the X-ray regime. However, if the X-ray emission has the same origin as that detected by Migliari et al. (2002), the highly-ionized iron lines seen in that observation would argue for a high temperature and bremsstrahlung X-ray emission, implying a hybrid thermal/non-thermal plasma in the jets.

4.2. *A radio/X-ray correlation*

We measured the total radio flux density enclosed in the regions selected for the X-ray data analysis (see Fig. 1) in the images of all 5 epochs, and the results are presented in Table 1. In 2003 July, when the X-ray reheating was observed, the radio flux was enhanced by a factor ~ 2 in the regions containing the X-ray emission, despite both the core emission and the integrated radio flux density in the jets being significantly less bright. This demonstrates that the radio emission is indeed related to the X-ray emission, and that there is some connection between the populations of emitting particles. The average fractional polarization does not seem to change significantly, implying that while the radio emission mechanism is synchrotron, the reheating does not change the degree of ordering of the magnetic field in the jets.

Migliari et al. (2005) presented evidence for variability of the arcsecond-scale X-ray jets in SS 433, on timescales of days and possibly hours. The X-ray jets are not persistent structures, as expected from the ~ 2 d lifetime of optically-emitting bullets close to the core (Vermeulen et al. 1993b). From our non-detections in 2006 February, we can put a lower limit on the duty cycle of any underlying shocks of ~ 10 d. This is further evidence for the transient nature of the X-ray jets and the reheating process that creates them.

4.3. *Energetics considerations*

The X-ray and radio fluxes in the selected X-ray emitting region in the eastern jet in 2003 July can be used to calculate the mass of particles required to generate the emission. Assuming a source distance of 5.5 kpc and a cylindrical emission region of length 1.46 arcsec and radius $1.98/2 = 0.99$ arcsec, we derive an emitting volume of $2.5 \times 10^{45} \, \mathrm{m}^3$.

4.3.1. *X-rays*

Assuming the X-ray emission to be thermal, we use the bremsstrahlung fit to the X-ray spectrum, which gave a temperature of 10.0 keV, and a 2–10 keV X-ray flux of $3.5 \times 10^{-13} \, \mathrm{erg \, cm^{-2} \, s^{-1}}$. The flux from thermal bremsstrahlung can be expressed as (Longair 1994)

$$F_{\mathrm{X}} = \frac{1.435 \times 10^{-40} Z^2 T^{1/2} g N N_{\mathrm{e}} V f}{4\pi d^2} \quad \mathrm{W \, m^{-2}}, \quad (1)$$

where Z is the mean atomic number of the atoms, T is the temperature, g is the Gaunt factor, and N and N_{e} are the ion and electron number densities. Assuming one proton for every electron, then $N = N_{\mathrm{e}}$. Thus we find a baryonic mass associated with the bremsstrahlung X-ray emission of

$$M_{\mathrm{brem}} = m_{\mathrm{p}} \left(\frac{4\pi d^2 F_{\mathrm{X}} V f}{1.435 \times 10^{-40} Z^2 T^{1/2} g} \right)^{1/2} \quad \mathrm{kg}, \quad (2)$$

where m_{p} is the proton mass. We do not know a priori the filling factor f of the emitting region. However, the predicted mass transfer rates are hyper-Eddington (King, Taam & Begelman 2000), so we can assume the accretion rate to be close to Eddington. Körding, Fender & Migliari (2006) found that a constant fraction of the liberated accretion power is injected into the jet. The kinetic power of the jet in SS 433, $(\gamma-1)\dot{M}c^2$, should therefore be of order L_{Edd}. The kinetic energy flux through the region where the X-ray counts are estimated is

$$L_{\mathrm{kin}} = (\gamma - 1) M_{\mathrm{brem}} c^2 \frac{vf}{l} = 10^{-3} L_{\mathrm{Edd}}, \quad (3)$$

where v is the jet speed, c is the speed of light, γ is the Lorentz factor, and l is the length of the emitting region along the direction of the jets. Rearranging and solving for the filling factor, using the fitted X-ray flux and temperature, a canonical Gaunt factor of 1.2, and assuming $Z = 1$ for a baryonic component consisting mainly of hydrogen, we find $f = 3 \times 10^{-3}$. To create the observed bremsstrahlung emission, this then gives an associated mass in baryons of $1.7 \times 10^{-5} M_{\odot}$.

4.3.2. *Radio*

Since the radio emission appears to be enhanced in the X-ray reheating region, we can attempt to estimate the mass required to emit the observed radio flux. Classic synchrotron minimum energy arguments, assuming that the electron energy distribution, $N(E) = \kappa E^{-p} dE$, extends from $E_{\mathrm{min}} = m_{\mathrm{e}}c^2$ up to $E_{\mathrm{max}} \gg m_{\mathrm{e}}c^2$, where m_{e} is the electron mass, give a total energy in relativistic particles of

$$W_{\mathrm{part}} = \left(\frac{4\pi d^2 S_{\nu} \nu^{(p-1)/2} \left(m_{\mathrm{e}}c^2\right)^{2-p}}{2.344 \times 10^{-25} (1.253 \times 10^{37})^{(p-1)/2}} \right)^{4/(5+p)}$$

$$\times \, [(p-2)a(p)]^{-4/(5+p)} \left(\frac{\mu_0(1+p)}{2Vf} \right)^{-\frac{1+p}{5+p}}, \quad (4)$$

where d is the source distance, μ_0 is the permeability of free space, and $a(p)$ is a slowly varying factor of p, equal to 0.45 for $p = 2.2$. We can integrate the electron energy distribution to find the total number of relativistic electrons responsible for the observed emission, via

$$N = \int_{E_{\mathrm{min}}}^{E_{\mathrm{max}}} \kappa E^{-p} \, dE \sim \frac{\kappa (m_{\mathrm{e}}c^2)^{1-p}}{(p-1)}. \quad (5)$$

By integrating to find the total energy in relativistic particles, we can solve for κ. We find

$$\kappa = \frac{W_{\mathrm{part}}(p-2)}{\eta V f(m_{\mathrm{e}}c^2)^{2-p}}. \quad (6)$$

Putting this all together, we can express the total mass of baryons associated with the synchrotron emission detected in the radio band as

$$M_{\mathrm{synch}} = V f N m_{\mathrm{p}} = \frac{W_{\mathrm{part}} m_{\mathrm{p}}(p-2)}{\eta m_{\mathrm{e}} c^2 (p-1)}. \quad (7)$$

Assuming one proton for every electron, a canonical spectral index $\alpha = -0.6$ ($p = 2.2$), a volume $V = 2.5 \times 10^{45} \, \mathrm{m}^3$ and a filling factor of $f = 3 \times 10^{-3}$ as derived above, we find a baryonic mass of $7.1 \times 10^{-10} M_{\odot}$ associated with the radio emission, variable within a factor ~ 5 for the range of spectral indices considered, i.e. $2.0 < p < 2.6$. The radio-emitting particles form a very small fraction of the total population in the jets. Most of the energy in the jets is dark (i.e kinetic, rather than radiative), in the absence of X-ray reheating.

5. THE MAGNETIC FIELD DIRECTION AND IMPLICATIONS FOR THE NATURE OF THE JETS

There has been extensive debate in the literature as to the continuous or discrete nature of the jets in SS 433. The presence of multiple peaks in the Doppler-shifted Hα line profiles of the source was taken as evidence for the discrete nature of the jets (Vermeulen et al. 1993b). Chakrabarti et al. (2002) discussed potential mechanisms for producing bullet-like ejections, and Chakrabarti et al. (2003) presented multiwavelength variability as evidence for such discrete bullets. However, the continuous core wings seen in VLBI images, the lack of structure on long baselines, and the tails of the bright radio knots which appeared to trace the nodding motion, argued for a more continuous flow, albeit with intermittent brightness enhancements (Vermeulen et al. 1993). The latter authors postulated the existence of a two-phase jet, with dense, cool optical-emitting clumps existing in a hot, continuous flow. The alignment of the magnetic field with the local velocity vector found by Stirling et al. (2004) was taken as further evidence for continuous jets.

We observed the magnetic field to be preferentially aligned with the ballistic velocity of the jet knots once they are sufficiently far outside the core to be unaffected by the enhanced Faraday rotation present close to the central binary. The discrepancy of our results with those of Stirling et al. (2004) is likely to be due to the higher signal-to-noise of our observations and the consequently increased number of precession periods out to which we can probe the magnetic field direction. Since the correlation only becomes clear $\gtrsim 1$ period out from the core

(Fig. 8), several precession cycles must be measured in order to detect the true correlation. Closer in, the increasing RM causes a rotation of the EVPAs and implied magnetic field directions, such that without an accurate RM map for the central regions, accurate measurements of the position angle cannot be made. However, Roberts et al. (2007) measured the magnetic field direction at 14.94 GHz, where the Faraday rotation, even for an RM of $596 \, \mathrm{rad} \, \mathrm{m}^{-2}$ (their highest measured value) is less than $15°$, which should not be sufficient to destroy the measured correlation. They found that the field was preferentially aligned along the kinematic model trace (the jet ridge line) between ~ 0.4 and 1 arcsec from the core. This suggests that the alignment of the magnetic field could change on moving beyond the core region, either because of contamination from the surroundings or the emission of the disc wind (Paragi et al. 1999; Blundell et al. 2001), or possibly reflecting a real change in the field orientation, perhaps due to shocks compressing the field at some distance from the core.

Stirling et al. (2004) derived the expected EVPA orientation for a longitudinal magnetic field along the plasma tube in the case of a smooth, continuous jet, finding it to be perpendicular to the apparent direction of the flux tube on the plane of the sky. Hence the inferred magnetic field direction would lie along the locus of the kinematic model trace, in contrast to the alignment with the ballistic velocity of the jet components (i.e. radially outward from the core) seen in our data beyond 1 arcsec. This argues against a smooth, continuous jet, since the absence of a component of the field perpendicular to the direction of ballistic motion implies that, to first order, the field at each point along the jet is not influenced by the direction of motion of the neighbouring points, such that each point is independent.

Stirling et al. (2004) also discussed the expected magnetic field configurations for a knotty jet composed of discrete components. If the ejecta compress the ISM through which they are moving, the ensuing shocks at the front surface will create a component of the magnetic field perpendicular to the velocity (e.g. Hughes, Aller & Aller, 1989). Alternatively, if the knots expand freely as they move through well-defined channels, Stirling et al. (2004) suggested that entrainment or stretching of the field lines would generate a component of the field parallel to the velocity vector. Due to the precession, such channels would appear as an evacuated layer on the surface of a cone, which, given the relatively long precession period of 162.5 d, we consider unlikely to remain empty for an entire precession cycle. We therefore consider alternative possible explanations for the observed field direction.

A preferential field orientation does not necessarily imply true uniformity of the magnetic field, since observations are only sensitive to the degree of ordering of the field in the plane perpendicular to the line of sight. An essentially irregular field can be made anisotropic via compression or shear effects, and depending on the orientation of the line of sight with respect to the plane of the shear or compression, can result in high degrees of observed polarization and apparent ordering of the field (Laing 1980). Velocity shear along the direction of motion and compression of the field via lateral expansion of an ejected knot could both give rise to an apparent

ordering of the field parallel to the local velocity vector, although this would come about in different ways. Shear would reduce the radial component of the field (perpendicular to the velocity vector) while leaving the longitudinal (parallel to the jet velocity) and toroidal components unchanged, whereas compression would amplify the longitudinal and toroidal components, without affecting the strength of the radial component.

The observed values of 20–30 per cent polarization along the jet locus are far from the theoretical maximum of $3(p+1)/(3p+7)$ (70 per cent for the canonical value of $p = 2.2$), implying some depolarization within the beam or along the line of sight. The jets are unresolved, so it is possible for the true geometry to comprise a number of emitting structures with different field alignments, with the emission-weighted average over the beam determining the observed orientation. Shock-compressed magnetic fields at the front surface of the knots could still be present, diluting the observed percentage polarization from a well-ordered field aligned parallel to the velocity, generated by lateral expansion and shearing effects. A possible analogy is to the hotspots of FR II radio galaxies (e.g. Dreher et al. 1987). A bowshock forms around the hotspot as it propagates outwards, with a field orientation perpendicular to the direction of motion at the head of the jet, and field lines swept back around the edges of the radio lobe, giving the field a "U"-shaped geometry. In our data, this entire structure is unresolved by the VLA. Close to the central source (< 0.4 arcsec; Roberts et al. 2007), the shock at the front surface is brightest, giving an observed field perpendicular to the velocity. As lateral expansion and velocity shear create a field well-aligned with the direction of motion, the parallel component begins to dominate and the observed field eventually becomes parallel to the velocity (i.e. the emission is dominated by long tails at the two sides of the "U", illuminated by the swept-back particles accelerated at the working surface). The corkscrew pattern observed for the SS 433 jets would then be caused by a superposition of many of these unresolved hotspot structures propagating outwards at different angles due to the precession of the jets.

Without resolving the emitting knots, it is impossible to derive the true field configuration and verify this scenario, which, while plausible, remains speculative. Detailed modelling of the true emissivity, magnetic field and velocity distributions across the source (as done for AGN by Laing & Bridle 2004) is impossible without further constraints, and is beyond the scope of this paper. The best approach would be to make deep observations of the jets at high frequencies in relatively extended array configurations, to attempt to resolve the individual emitting knots well outside the core, and the variation in magnetic field orientation across them. Furthermore, high frequency observations, where the data are less affected by Faraday rotation, are warranted to probe the inner regions, to ascertain whether the magnetic field direction remains correlated with the local velocity close to the central binary. Whatever the actual field configuration, the observed correlation of the magnetic field direction with the local velocity vector (Section 3.2.1) implies that the jet is unlikely to be a continuous flux tube, and is more likely to be composed of a series of discrete, unconnected, radio-emitting bullets, as seen in VLBI images

(e.g. Mioduszewski et al. 2003; Paragi et al. 1999).

6. CONCLUSIONS

With the deepest radio polarization image to date, we have measured the magnetic field direction in the extended jets, finding it to be aligned with the local velocity vector. This suggests that the jets are likely to be composed of discrete bullets, rather than being continuous flux tubes. We confirm the depolarization region surrounding the core which was noted by Stirling et al. (2004). We also see evidence for regions of anomalous, polarized emission away from the kinematic model trace in images from five different epochs, seen also in older observations from the literature. Such anomalous emitting structures appear to be the rule, rather than the exception in this system. The magnetic field in these anomalous regions is observed to be aligned perpendicular to the velocity vector away from the core, indicating possible shock compression of the field. Alternatively, shearing motions at the interface of the jet and ambient medium could cause the observed large-scale ordering of the magnetic field.

For the first time, we have studied the correlation between the radio and X-ray emission in the arcsecond-scale jets of SS 433. The radio emission is enhanced in the presence of X-ray jets. The arcsecond-scale X-ray jets are transient, and their presence does not correlate with the flux density of the core. We saw no evidence for a faster, underlying flow energising individual emitting knots. If it exists in this system, it was not active during these observations. The core shows evidence for highly-ionised iron lines, at the redshifts predicted by the kinematic model. We cannot confirm at any significant level the existence of the iron line previously seen in the spatially resolved X-ray jets, because of the very bright and highly piled-up core which makes the measurement of the weak features in the jet spectra, such as the lines, very difficult. The measured X-ray flux is consistent with a single spectral index of -0.8 running all the way from the radio band to the X-rays. While we cannot significantly distinguish between a bremsstrahlung and a power-law origin for the X-rays in the extended jets, bremsstrahlung seems more likely given the highly-ionised iron lines observed previously in the jets, which would suggest that the X-rays are not simply the tail of the radio synchrotron spectrum.

REFERENCES

Abell G. O., & Margon B. 1979, Nature, 279, 701
Begelman M. C., Hatchett S. P., McKee C. F., Sarazin C. L., & Arons J. 1980, ApJ, 238, 722
Blundell K. M., & Bowler M. G. 2004, ApJ, 616, L159
Blundell K. M., & Bowler M. G. 2005, ApJ, 622, L129
Blundell K. M., Mioduszewski A. J., Muxlow T. W. B., Podsiadlowski P., & Rupen M. P. 2001, ApJ, 562, L79
Chakrabarti S. K., Pal S., Nandi A., Anandarao B. G., Mondal S., 2003, ApJ, 595, L45
Chakrabarti S. K., Goldoni P., Wiita P. J., Nandi A., Das S., 2002, ApJ, 576, L45
Dreher J. W., Carilli C. L., Perley R. A., 1987, ApJ, 316, 611
Fabian A. C., & Rees M. J. 1979, MNRAS, 187, 13P
Fender R., Wu K., Johnston H., Tzioumis T., Jonker P., Spencer R., & van der Klis M. 2004, Nature, 427, 222
Fomalont E. B., Geldzahler B. J., & Bradshaw C. F. 2001, ApJ, 553, L27
Greisen, E.W. 1983, AIPS Memo 27
Heavens A. F., Ballard K. R., & Kirk J. G. 1990, MNRAS, 244, 474
Hjellming R. M., Johnston K. J., 1981, Nature, 290, 100
Hughes P. A., Aller H. D., & Aller M. F. 1989, ApJ, 341, 54
King A. R., Taam R. E., Begelman M. C., 2000, ApJ, 530, L25
Körding, E. G., Fender R. P., Migliari S., 2006, MNRAS, 369, 1451
Laing R. A., 1980, MNRAS, 193, 439
Laing R. A., Bridle A. H., 2004, MNRAS, 348, 1459
Lockman F. J., Blundell K. M., & Goss W. M. 2007, MNRAS, 381, 881
Longair M. S., 1994, High energy astrophysics. Vol.2: Stars, the galaxy and the interstellar medium. (2nd ed.; Cambridge: Cambridge University Press)

Margon B., Grandi S. A., Stone R. P. S., & Ford H. C. 1979, ApJ, 233, L63
Marshall H. L., Canizares C. R., & Schulz N. S. 2002, ApJ, 564, 941
Migliari S., Fender R., & Méndez, M. 2002, Science, 297, 1673
Migliari S., Fender R. P., Blundell K. M., Méndez, M., & van der Klis M. 2005, MNRAS, 358, 860
Milgrom M. 1979, A&A, 76, L3
Mioduszewski A. J., Rupen M. P., Walker R. C., & Taylor G. B. 2003, BAAS, 35, 1254
Paragi Z., Vermeulen R. C., Fejes I., Schilizzi R. T., Spencer R. E., & Stirling A. M. 1999, A&A, 348, 910
Roberts D. H., Wardle J. F. C., Lipnick S. L., Selesnick P. L., & Slutsky S. 2007, ApJ, accepted (arXiv:0712.2005)
Spencer R. E., & Waggett P. 1984, in Proc. IAU Symp. 110, VLBI and Compact Radio Sources. Kluwer, Dordrecht, p.297
Stirling A. M., Jowett F. H., Spencer R. E., Paragi Z., Ogley R. N., & Cawthorne T. V. 2002, MNRAS, 337, 657
Stirling A. M., Spencer R. E., Cawthorne T. V. & Paragi Z. 2004, MNRAS, 354, 1239
Vermeulen R. C., Schilizzi R. T., Spencer R. E., Romney J. D., & Fejes I. 1993, A&A, 270, 177
Vermeulen R. C. et al. 1993b, A&A, 270, 204
Watson M. G., Stewart G. C., King A. R., Brinkmann W., 1986, MNRAS, 222, 261